Geophysical Research Letters

RESEARCH LETTER
10.1029/2019GL083283

Key Points:
- Whistler mode waves are detected by MMS spacecraft in the vicinity of the near-Earth neutral line in the magnetotail
- The parallel propagation velocity of the whistler wave is in the range (1-5 keV) of the inverse slope of the field-aligned crescent
- The whistler waves are driven by the field-aligned crescent-like electrons through the Landau resonance interaction

Supporting Information:
- Supporting Information S1

Correspondence to:
L. Dai,
ldai@spaceweather.ac.cn

Citation:
Ren, Y., Dai, L., Li, W., Tao, X., Wang, C., Tang, B., et al. (2019). Whistler waves driven by field-aligned streaming electrons in the near-Earth magnetotail reconnection. *Geophysical Research Letters*, *46*, 5045–5054. https://doi.org/10.1029/2019GL083283

Received 11 APR 2019
Accepted 10 MAY 2019
Accepted article online 16 MAY 2019
Published online 30 MAY 2019

©2019. American Geophysical Union. All Rights Reserved.

Whistler Waves Driven by Field-Aligned Streaming Electrons in the Near-Earth Magnetotail Reconnection

Y. Ren[1], L. Dai[1], W. Li[2], X. Tao[3], C. Wang[1], B. Tang[1], B. Lavraud[4], Y. Wu[3], J. L. Burch[5], B. L. Giles[6], O. Le Contel[7], R. B. Torbert[8], C. T. Russell[9], R. J. Strangeway[9], R. E. Ergun[1,10], and P.-A. Lindqvist[1,11]

[1]State Key Laboratory of Space Weather, National Space Science Center, Chinese Academy of Sciences, Beijing, China, [2]Center for Space Physics, Boston University, Boston, MA, USA, [3]CAS Key Laboratory of Geospace Environment, Department of Geophysics and Planetary Sciences, University of Science and Technology of China, Hefei, China, [4]Institut de Recherche en Astrophysique et Planétologie, Université de Toulouse, CNRS, UPS, CNES, Toulouse, France, [5]Southwest Research Institute, San Antonio, TX, USA, [6]NASA Goddard Space Flight Center, Greenbelt, MD, USA, [7]Laboratoire de Physique des Plasmas, CNRS/Ecole Polytechnique/Sorbonne Université/Université Paris-Sud/Observatoire de Paris, Paris, France, [8]Department of Physics, University of New Hampshire, Durham, NH, USA, [9]Earth and Planetary Sciences, University of California, Los Angeles, Los Angeles, CA, USA, [10]Department of Astrophysical and Planetary Sciences, University of Colorado Boulder, Boulder, CO, USA, [11]Space and Plasma Group, Royal Institute of Technology, Stockholm, Sweden

Abstract We analyze Magnetospheric Multiscale Mission observations of whistler waves and associated electron field-aligned crescent distribution in the vicinity of the magnetotail near-Earth X-line. The whistler waves propagate outward from the X-line in the neutral sheet. The associated field-aligned streaming electrons exhibit a crescent-like shape, with an inverse slope ($\mathrm{d}f/\mathrm{d}|v_{||}| > 0$) at 1–5 keV. The parallel phase velocity of the waves is in the range (1–5 keV) of the inverse slope of the field-aligned crescents in the velocity space. We demonstrate that the observed whistler waves are driven by the electron field-aligned crescents through Landau resonance. The cyclotron resonance is at the high-energy tail with negligible free energy of pitch angle anisotropy in these events.

1. Introduction

Magnetic reconnection converts magnetic energy into plasma kinetic and thermal energies. During energy conversion of reconnection, non-Maxwellian distributions of electron are produced, providing free energy to excite plasma waves. Investigations of electron-scale plasma waves may provide a valuable perspective on the kinetic-process associated with the electron diffusion region.

One particular type of electron-scale plasma waves intensively studied in reconnection is the whistler emission. Whistler mode waves have been observed prior to and during the magnetotail reconnection using Cluster data (Wei et al., 2007). At the dayside magnetopause reconnection, whistler mode waves have been reported in the separatrix region from Cluster (Graham et al., 2016) and recent Magnetospheric Multiscale Mission (MMS) observations (Le Contel, Retinò, et al., 2016; Wilder et al., 2016, 2017, Yoo et al., 2018). In the magnetotail, Cluster observations show that whistler waves occur near the separatrix region and the magnetic pileup region of downstream flows (Huang et al., 2016). Near the X-line of reconnection, whistler mode waves have been observed as well (Burch et al., 2018; Cao et al., 2017; Li et al., 2018; Tang et al., 2013). With unprecedented high-resolution measurements, MMS has demonstrated the existence of whistler emissions near and within the electron diffusion region (Burch et al., 2018; Cao et al., 2017).

The generation of the whistler mode waves is important for understanding wave-particle interactions in reconnection. Normally, whistler mode emissions are excited by the cyclotron resonance and Landau resonance with electrons (Kennel, 1966). The $n = \pm 1$ cyclotron resonance condition is $\omega - k_{||}v_{||} = \pm\Omega_e^-$, usually corresponding to free energy in the anisotropic electron distribution with respect to pitch angles (Kennel, 1966). The $n = 0$ Landau resonance condition (also named Cerenkov resonance) is $\omega - k_{||}v_{||} = 0$, corresponding to free energy in an inverse slope ($\mathrm{d}f/\mathrm{d}|v_{||}| > 0$) in the parallel velocity distribution (An et al., 2016; Goldman et al., 2014; Kennel, 1966; Li et al., 2016).

Until now, whistler emissions observed in reconnection are mostly generated from cyclotron resonance with the free energy in the electron temperature anisotropy ($T_\perp/T_{||} > 1$) (Burch et al., 2018; Cao et al., 2017; Graham et al., 2016; Li et al., 2018; Le Contel, Retinò, et al., 2016; Tang et al., 2013; Wilder et al., 2017; Yoo et al., 2018). Studies on whistler generation from Landau resonance are rather limited. A few observations from Cluster and Geotail suggest that field-aligned electron beams in reconnection may excite whistler emissions (Huang et al., 2016; Zhang et al., 1999; Zhou et al., 2011). But the generation mechanism was difficult to identify due to the lack of high cadence measurements of electron distributions in past studies. Recent two-dimensional particle-in-cell simulation shows that electron beams can drive whistler instability in separatrix regions of reconnection (Fujimoto, 2014). Using high-resolution electron distribution data from MMS, here we present an event study demonstrating the whistler generation from Landau resonance near magnetic reconnection. One breakthrough discovery made by recent MMS observations is the electron crescent-shape distributions parallel to the magnetic field in the electron diffusion region (Burch et al., 2016). Such field-aligned electron crescents might evolve from perpendicular electron crescents in the center of the electron diffusion region (Burch et al., 2016). Field-aligned electron beam-like distributions are known from observations and simulations of magnetotail reconnection (e.g., Hoshino et al., 2001; Nagai et al., 1998). Our investigation is of particular interest since field-aligned electron crescents and beams generally may lead to parallel velocity distributions suitable for Landau resonance.

2. Observations and Analysis

The MMS spacecraft are located in the magnetotail at (−24.3, −1.3, 4.6) *Re* GSM (geocentric solar magnetic coordinate systems) around 2200 UT on 3 July 2017 in this event. Our observations consist of the direct current and alternating current coupled measurements of magnetic field from the fluxgate magnetometer (Russell et al., 2016) and search coil magnetometer (Le Contel, Leroy, et al., 2016), the direct current coupled electric field measurements (Ergun et al., 2016; Lindqvist et al., 2016; Torbert et al., 2016), the plasma measurements from the Fast Plasma Investigation (FPI; Pollock et al., 2016) and the Energetic Particle Detector (Blake et al., 2016).

2.1. The 3 July 2017 Reconnection Event

Figure 1 is the overview of the reconnection event from 2153 to 2210 UT from MMS1. The magnetic field and ion velocity are shown in the GSM coordinate system. The GSM is close to the LMN coordinate [with **N** in (0.07,−0.04,0.99) GSM and **M** in (−0.07, 0.996, 0.05) GSM] as determined from the minimum variance analysis (21:56–22:06 UT) of the magnetic field. The magnetotail reconnection is identified from the reversal of the magnetic field B_z accompanied with plasma flow velocity v_x in GSM around 2201! UT near the neutral sheet (Figure 1a and 1b). Such reversal in B_z and v_x is the signal as the spacecraft crossing a tailward retreating X-line (Dai et al., 2011, 2015; Hones, 1976; Zhang et al., 2010, 2015), as shown in the schematic in Figure 1i. From 2154 to 2157 UT, MMS observes typical tenuous plasma sheet ions and electrons from 1 to 20 keV (panels e and f). From 215720 to 220400 UT, MMS is close to the neutral sheet and the X-line, encountering the plasma sheet boundary layer (PSBL). This is particularly clear in the electron energy spectra (panel f) showing a temperature of about 500 eV. Tail lobe plasma populations are not observed near the X-line. This is because the near-Earth X-line, unlike the tail-lobe reconnection, is supported and surrounded by plasma inflow from the PSBL. The near-Earth X-line is reconnecting inside the plasma sheet (and PSBL) and not yet with the lobes. After 2204 UT, MMS reenters the earthward reconnection exhaust characterized with tenuous plasmas from the plasma sheet. The earthward reconnection outflow observed by MMS has fully developed to Alfven speed near 2204–2205 UT.

The interval of interest is around 21:57 UT. Observations of whistler wave trains are marked by vertical dashed lines. The dominant magnetic field component is B_x less than 15 nT, suggesting that the MMS is in the magnetotail current layer. From 215700 to 215730 UT, the B_y exhibits an enhancement as large as +5 nT. Near the X-line during 2200–2201 UT, MMS observed a corresponding Hall electric field E_z of −5 mV/m. The Hall electric field is identified near the X-line center where its value is expected maximal. The $+B_y$ combined with the Hall electric field E_z indicates that MMS1 encounters the ion diffusion region of the collisionless reconnection. The ratio of Hall electric field (5 mV/m) to the Hall magnetic field 5 nT is about 1,000 km/s, around 1.3 Alfven speed V_A. In general, the spatial scale of the Hall fields is about the current layer thickness (the ion scale) in the normal direction. The spatial scale and the ratio $\mathbf{E}_{\mathrm{Hall}}/\mathbf{B}_{\mathrm{hall}}$ of the Hall fields is consistent with a Kinetic Alfven wave nature as shown in theoretical results (Dai, 2018, 2009;

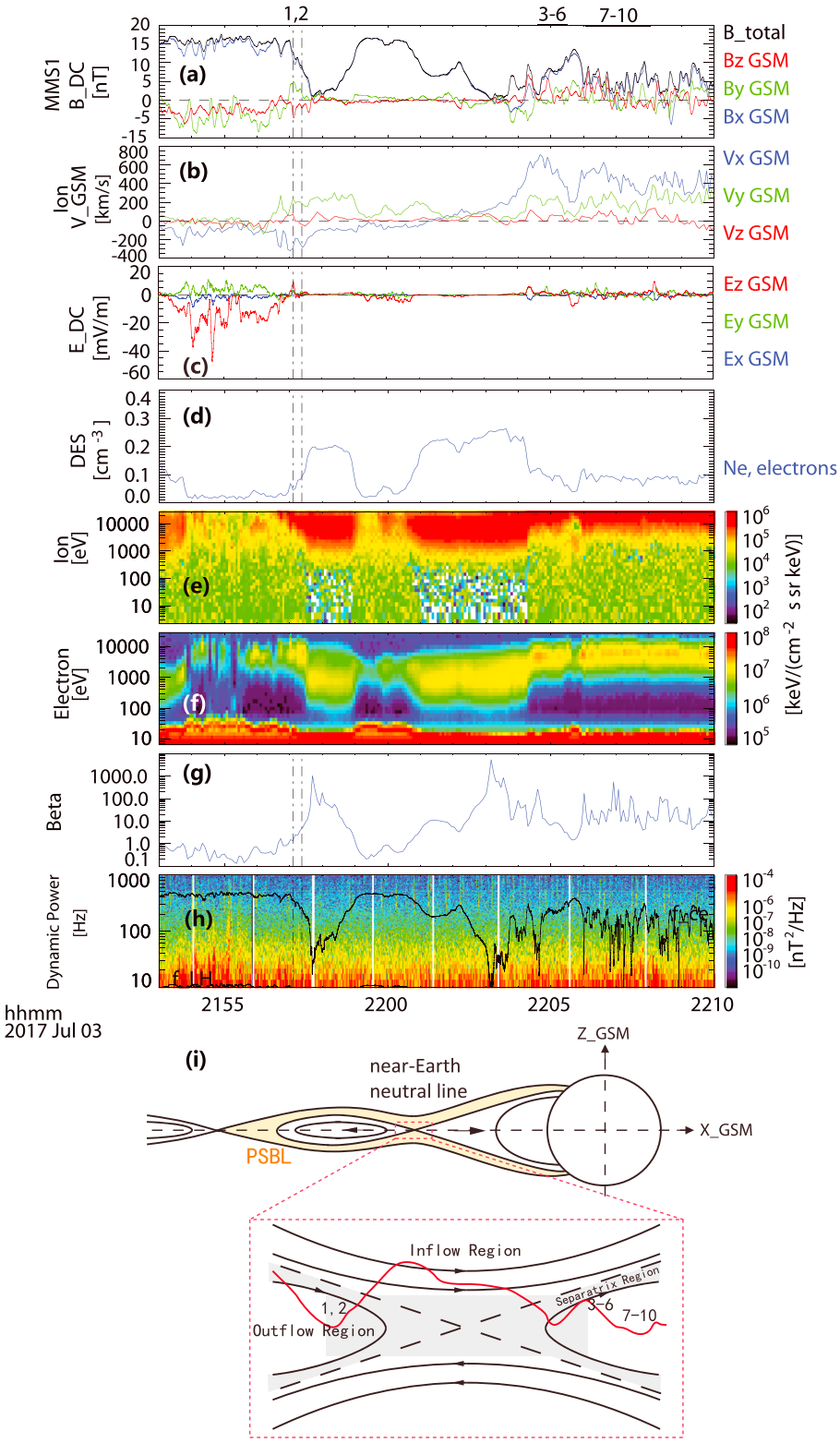

Figure 1. MMS 1 observations on 3 July 2017 of near-Earth magnetic reconnection region. (a) The magnetic field; (b) ion bulk flow velocity in GSM; (c) the electric field in GSM; (d) the electron number density; (e) ion omnidirectional differential energy fluxes; (f) electron omnidirectional differential energy fluxes; (g) plasma beta; (h) the dynamic power spectra of magnetic field; (i) the schematic of the MMS trajectory across a tailward moving X-line. GSM = geocentric solar magnetic coordinate systems.

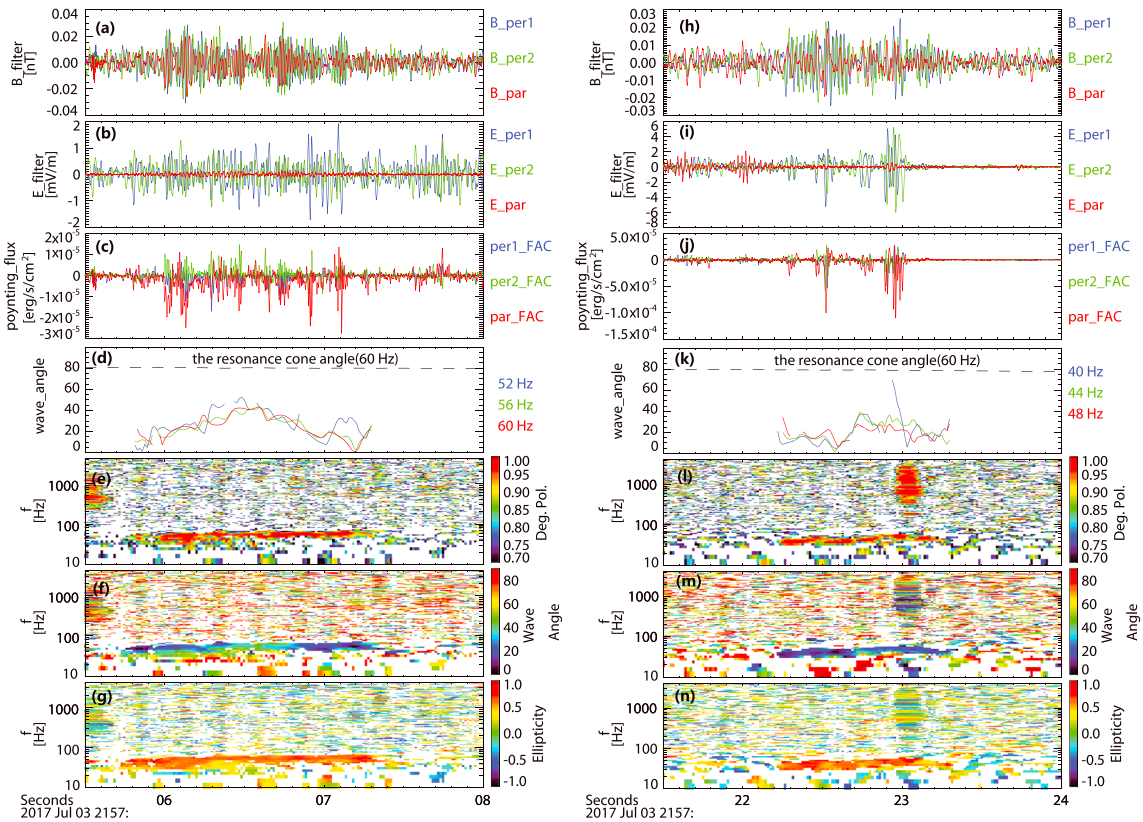

Figure 2. Properties of whistler waves in events 1 and 2. The left panels, (a)–(g), show for event 1, (a) the filtered three magnetic field components in the FAC system; (b) the filtered three electric field components; (c) the wave Poynting flux from the filtered electric field and magnetic field components; (d) the wave normal angle at selected frequencies, (e) the degree of polarization of the wave, (f) the spectra of the wave normal angle with respect to **B**; and (g) the ellipticity of the waves. +1 corresponds to a right-hand circular polarization. In the same format of (a)–(g), panels (h)–(n) show the wave properties in event 2.

Dai et al., 2017), particle-in-cell simulations (Huang et al., 2018), and in situ observations (Duan et al., 2016, 2017; Zhang et al., 2017). Around 21:57 UT, the ion flow (200–300 km/s) is much less than the Alfven speed (740 km/s). This is expected as the ion acceleration is not yet fully developed in the ion diffusion region.

The power spectral densities of alternating current magnetic fields is shown in Figure 1h. In the next section, we analyze the whistler emission identified in the intervals 1 and 2. The first dashed line (event 1) indicates the 1.5 s around 21:57:06 UT. The second dashed line (event 2) indicates the 1 s of enhancement of whistler waves around 21:57:22 UT. Unlike many previous observations of continuous power spectra of whistler wave, the wave activities occurred within very short (1 s) and discrete intervals in our event. Whistler waves are also identified in the intervals 3–10 (supporting information). Whistler waves in these intervals are in the magnetic field piled-up region of the ion exhaust (Fu et al., 2014). The whistlers in the intervals 3–10 are probably produced by electron temperature anisotropy.

2.2. Whistler Mode Waves

Whistler emissions are right-hand polarized electromagnetic waves at frequencies $\Omega_i \ll \omega < \Omega_e$ (Artemyev et al., 2016; Cattell et al., 2008; Tsurutani & Smith, 1977). Figure 2 shows the properties of the observed whistler waves in the intervals 1 and 2. Panel (a), (b) and (h), (i) present the waveform of the electric fields and magnetic fields in the FAC (magnetic field-aligned coordinate system with the magnetic field direction obtained from the flugate magnetometer survey data). The waveform is filtered with a bandpass (30–100 Hz) containing the power of identified whistler emissions. The wave electric field and magnetic field is from the 8,192 S/s search coil magnetometer and EDP data. For both events, the peak-to-peak amplitude of the wave magnetic field is about 0.04 nT. The peak-to-peak amplitude of the wave electric field is more dynamic, varying from 2 mV/m in event 1 to as large as 10 mV/s occasionally in event 2. From 21:57:23 to 21:57:23.2 UT, there is very weak electric field and small E/B associated with the wave magnetic power near 40 Hz. This may be due to change of plasma environment and associated free energy. The wave Poynting flux calculated

from the filtered waveform data in the FAC for both events is shown in panels (c) and (j). In both events, the field-aligned component (red) of the Poynting flux is dominant and antiparallel to the magnetic field for most of the time. Considering the geometry in Figure 1i, the wave group velocity in our events is outward from the X-line most of the time. The magnitude of whistler Poynting flux is comparable to that in the radiation belt but less than that of certain large-amplitude whistler mode waves (Wilson et al., 2011).

The degree of polarization, the wave normal angle, and the ellipticity of the waves in both events are presented in panels (d)–(g) and (k)–(n). The degree of polarization and the ellipticity are close to 1 (red), indicating that the identified waves are purely right-handed circular whistler waves (Huang et al., 2016; Narita, 2017). The direction of the wave vector k is determined by the minimum variance analysis of $\delta\mathbf{B}$ (Sonnerup & Scheible, 1998) with a time window 0.2 s. The wave normal angle, defined as the angle between the propagation direction ($\mathbf{k}$) and the ambient magnetic field, varies between 0° and 50° in both events. The wave normal angle is less than the resonance cone angle $arcos(\omega/\Omega_e)$ (around 80°) in our events.

2.3. Electron Distributions

The electron pitch angle distribution, the 2-D distribution functions, and the 1-D parallel velocity distribution during the whistler waves in the events are provided in Figure 3. The 2-D distribution data are presented in a 150×150 data grid in the distributed MMS data. To reduce the statistical noise, the distribution is averaged over 0.06 s and smoothed over a 15 X 15 data grid. The 1-D average parallel velocity distribution $f_e(v_\parallel)$ is obtained by an average from $v_\perp = -3 \times 10^4$ km/s to $v_\perp = 3 \times 10^4$ km/s.

In event 1 (Figures 3a and 3b), the electron differential energy flux shows an enhancement at pitch angle 150–180° (antiparallel) in the energy 1–5 keV. Electrons in the parallel direction (0–30°) also increase, but the intensity is much weaker. The superthermal electron fluxes in the range of 40–260 keV in event 1 is shown in Figure 3b.

At 21:57:06.328, the 2-D distribution functions in Figure 3c shows a weak crescent-like beam around 2.5–4 $\times 10^4$ km/s in the antiparallel direction. The crescent-like beam distribution is characterized by a narrow spread (1.0×10^4 km/s) in the parallel direction and a wide thermal spread (3.2×10^4 km/s) in the perpendicular direction. The field-aligned crescent spans about 45° with respect to the $-\mathbf{B}$ direction, extending from $v_\perp = -4.0 \times 10^4$ to $v_\perp = 3.0 \times 10^4$ km/s. About 0.15 s later at 21:57:06.468, the crescent-like beam distribution in the antiparallel direction is still observed. Figure 3d shows the crescent-like beam at -2.0×10^4 to -4.0×10^4 km/s. The field-aligned streaming speed of the crescent-like beam ($\sim 4.0 \times 10^4$km/s) is close to the electron Alfven speed ($\sim 4.6 \times 10^4$km/s). As shown in the 1-D distribution functions from Figure 3c, the field-aligned crescent-like beam corresponds to a bump distribution with an inverted slope ($\mathrm{d}f/\mathrm{d}|v_{||}| > 0$; around 1.8–3.9 $\times 10^4$ km/s or 0.9–4.4 keV) in the antiparallel (red) direction.

Event-2 is closer to the X-line than event-1. The electron flux in 1–5 keV and 40–260 keV both show enhancements in the antiparallel direction in Figures 3e and 3f. At 21:57:22.390 UT, the electron exhibits a crescent-like beam distribution in the antiparallel direction in the 2-D distribution in Figure 3g. The crescent creates the inverse slope ($\mathrm{d}f/\mathrm{d}|v_{||}| > 0$) around -1.5×10^4 to -2.2×10^4 km/s (0.6–1.3 keV) in the antiparallel direction in the 1-D parallel velocity distribution. About 0.4 s later at 21:57:22.796 UT, the electron crescent-like beam varies significantly on the timescale of 0.1 s. From the 1-D velocity distribution, we can still see the inverted slope ($\mathrm{d}f/\mathrm{d}|v_{||}| > 0$) around -2.2×10^4 to -2.6×10^4 km/s (1.3–1.9 keV) in the antiparallel direction (red) corresponding to the crescent-like beam distribution in Figure 3h.

2.4. The Wave Generation

From the linear theory perspective, the generation of whistler waves is due to free energy of the electron distributions at resonances $\omega - k_\parallel v_\parallel = -n\Omega_e$ (Kennel, 1966). The whistler growth rate γ for cold electrons ($V_{\text{resonance}} > V_{\text{thermal}}$), as in equation (4.5) in Kennel (1966), is due to the superposition of each resonance ($n = 0, \pm 1, \pm 2...$):

$$\gamma = \pi^2 \Omega_e \left|\frac{\omega}{k}\right| \int_0^\infty v_\perp^2 \mathrm{d}v_\perp \int_{-\infty}^\infty \mathrm{d}v_\parallel \sum_n \delta\left(v_\parallel - \frac{\omega + n\Omega_e}{k_\parallel}\right) A_n G, \tag{1}$$

where n is the resonance number in the resonance condition, A_n is the positive and definite weighting function for a given resonance n, Ω_e is the absolute value of gyrofrequency and its sign is positive. The most important resonance is the $n = \pm 1$ cyclotron resonance and the $n = 0$ Landau resonance (Kennel, 1966), with the approximated factor G as follows:

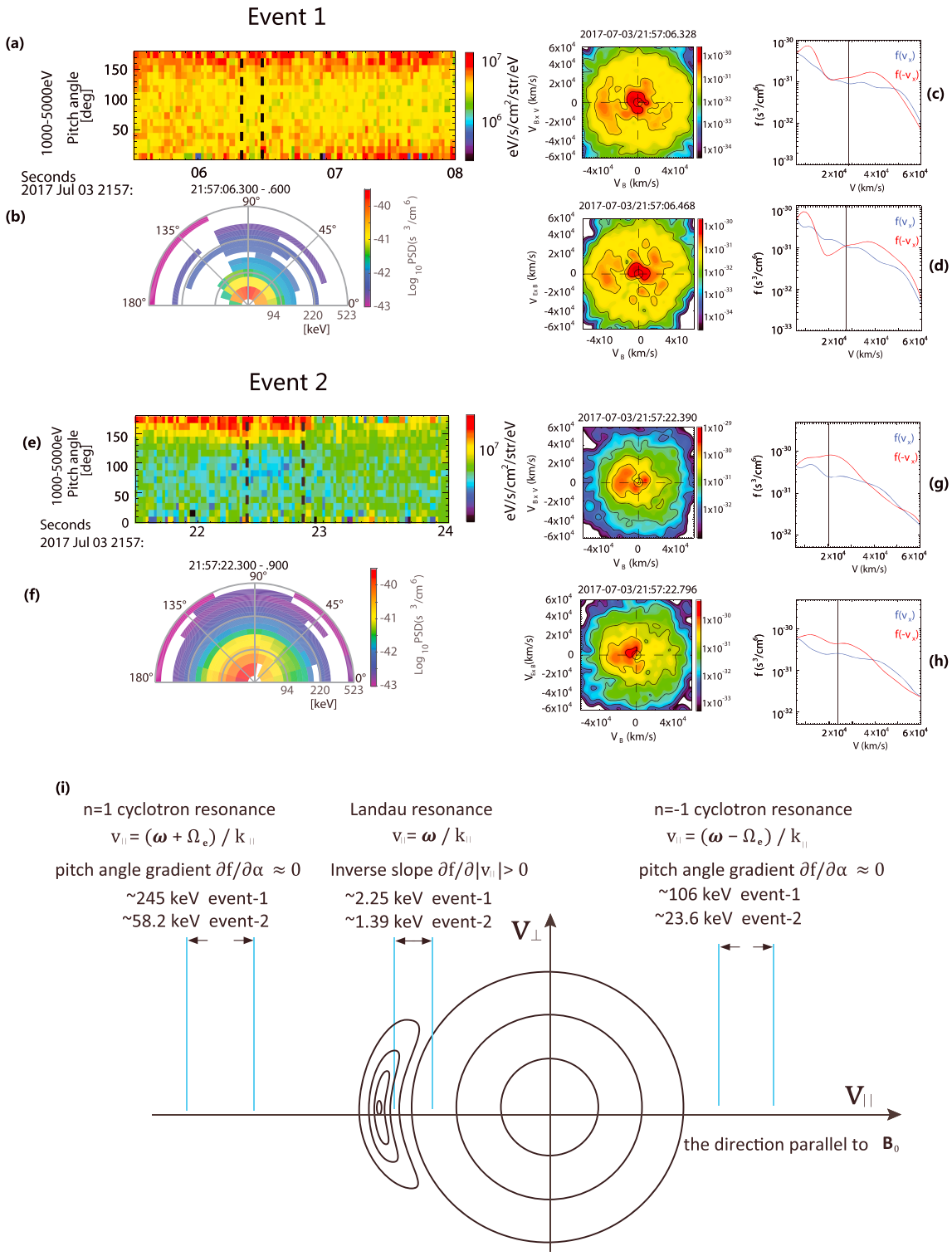

Figure 3. The electron velocity distributions and the analysis of whistler wave generation. (a, b) The electron pitch angle distribution at energy 1–5 and 40–260 keV in event 1. (c, d) The 2-D electron distribution and the parallel velocity distribution at the time indicated by the first dashed line in event 1. The vertical lines in the parallel distribution indicate the wave-parallel propagation velocity obtained from $\delta E_{\perp}/\delta B_{\perp}$. (e–h) The electron pitch angle and velocity distribution in event 2. (i) The schematic of the whistler wave generation by the Landau resonance.

$$G_{n=0} \approx (k_{||} v_{\perp}/\omega)(\partial F/\partial v_{||})|_{v_{||}=(\omega)/k_{||}}, \tag{2}$$

and

$$G_{n=\pm 1} \approx (-k_{||}/\omega)(\partial F/\partial \alpha)|_{v_{||}=(\omega+n\Omega_e)/k_{||}}, \tag{3}$$

F is the distribution function normalized by the number density (f/N), α is the pitch angle of the electron.

The factor G represents the free energy for waves at each resonance. As indicated in equations (2) and (3), the free energy source for the $n = 0$ Landau resonance is an inverse slope ($\mathrm{d}F/\mathrm{d}|v_{||}| > 0$) near the resonance velocity in the distribution. The free energy source for the $n = \pm 1$ cyclotron resonance is a pitch angle anisotropy $\partial F/\partial \alpha > 0$ near the corresponding resonance velocity in the distribution. In our observations, the cold plasma assumption ($V_{\mathrm{resonance}} > V_{\mathrm{thermal}}$) is not satisfied. The coefficients in front of G for the growth rate of each resonance in equation (1) should be modified due to hot plasma effect. The cold plasma assumption, however, does not affect the imaginary part of the dielectric tensor. The results of equations (2) and (3) are expected to be useful for a qualitative evaluation of the free energy at $n = 0$ and $n = \pm 1$ resonance.

The resonance energy and free energy for $n = 0$ and $n = \pm 1$ resonance in the events is summarized in the schematic Figure 3i. The $n = 0$ resonance velocity $v_{||} = \omega/k_{||}$ is estimated through the Maxwell equation from the perpendicular wave field as $\omega/k_{||} = \frac{|\delta E_{\perp}|}{|\delta B_{\perp}|}$ (e.g., Dai et al., 2014). The root-mean-square of the field with a 0.05-s window has been used to compute the wave amplitude. The obtained Landau resonance velocity ($\omega/k_{||}$) in event 1 is from -2.7×10^4 to -2.9×10^4 km/s, corresponding to a $1/2m_e v_{||}^2$ at 2.25 keV. This value is similar to that obtained from the singular value decomposition method (Santolík et al., 2003). In event 2, the Landau resonance velocity is -2.0×10^4 to -2.3×10^4 km/s, corresponding to a parallel energy $1/2m_e v_{||}^2$ of 1.4 keV. The $n = 0$ resonance velocity is marked as vertical lines in the 1-D distribution in Figures 3c, 3d, 3g, and 3h. The $n = 0$ resonance velocity is in the middle of the inverse slope (more particles in the higher energy) associated with the crescent-like beam. This inverse slope provides the free energy for waves to grow from Landau resonance. As indicated in the 2-D and 1-D distributions, the electron phase space density (δf) participating the Landau resonance near the inverse slope is on the order of 10^{-31} s^3/cm^6.

We further examine the resonance energy and free energy for the $n = \pm 1$ cyclotron resonance. The $n = 1$ resonance velocity corresponds to an energy $1/2m_e v_{||}^2$ of 245 keV (considering relativistic energy correction) in event 1 and 58 keV in event 2 in the antiparallel direction. The $n = -1$ resonance velocity corresponds to an energy $1/2m_e v_{||}^2$ of 106 keV in event 1 and 23 keV in event 2 in the parallel direction. For event 1, we find no free energy of positive $\partial F/\partial \alpha$ at the $n = \pm 1$ resonance energy. In event 2, there is some pitch angle anisotropy $\partial F/\partial \alpha > 0$, but the electron phase space density (δf) participating in the $n = 1$ resonance is less than 10^{-40} s^3/cm^6. This δf is 9 orders of magnitude smaller than that of Landau resonance. For the $n = -1$ resonance in event 2, the δf is small (10^{-36} s^3/cm^6) as well. The qualitative estimate suggests that the free energy for $n = \pm 1$ cyclotron resonance is negligible for the whistler waves in these events.

We evaluate the growth rate of whistler waves from the Waves in Homogeneous Anisotropic Magnetized Plasma modeling of hot plasmas. The results are shown in Figure 4. The modeled distribution for event 1 in Figure 3d is a superposition of four populations with parameters as, $B = 12$ nT, $n_e = 0.06$ cm^{-3}, $n_o = 1.2n_e$, $T_{eo\perp} = T_{eo||} = 3{,}000$ eV, $V_d = 0$ km/s, $n_1 = 0.15n_e$, $T_{e1\perp} = 3{,}000$ eV, $T_{e1||} = 400$ eV, $V_{d1} = -3.83 \times 10^4$ km/s, $n_2 = -0.3n_e$, $T_{e2\perp} = 3{,}000$ eV, $T_{e2||} = 400$ eV, $V_{d2} = -1.46 \times 10^4$ km/s, $n_3 = -0.05n_e$, $T_{e3\perp} = 1{,}000$ eV, $T_{e3||} = 400$ eV, $V_{d3} = -3.24 \times 10^4$ km/s. V_d are drift velocities along the magnetic field. The addition of negative density populations is interpreted as electron density holes. As seen from Figure 4, there is significant growth rate $\gamma/\Omega_e \sim 0.005$ for whistler waves that propagate in the antiparallel direction (showing negative wave frequency). The parameter space ($\omega/\Omega_e \sim 0.11$–$0.17$, wave normal angle $\theta \sim 0$–$50°$ with respect to $-\mathbf{B}$) of the whistler waves in observations is close to the regime of maximal growth rate. The maximal growth rate (Figure 4e) in the modeling is 0.006 with a wave normal angle near 51° with respect to $-\mathbf{B}$. This wave normal angle has some small deviations with the observations. The uncertainty in the observed wave properties, the observed distributions, and in the modeling distribution, all may contribute to the small deviations in panel (f). The $k_{||} V_{\mathrm{th}}^e/\Omega_e$ is 0.2–0.3 in the parameter space in Figure 4f, corresponding to a wavelength of 320–480 km. This modeling result is close to the observation of the wavelength (400 km), characterized with a frequency of 50 Hz and a parallel speed of 2×10^4 km/s. The growth rate of whistler waves diminish accordingly once we try to decrease the density of electron crescents. The numerical modeling results indicate that whistler waves are driven by the field-aligned crescents-like beam through Landau resonance.

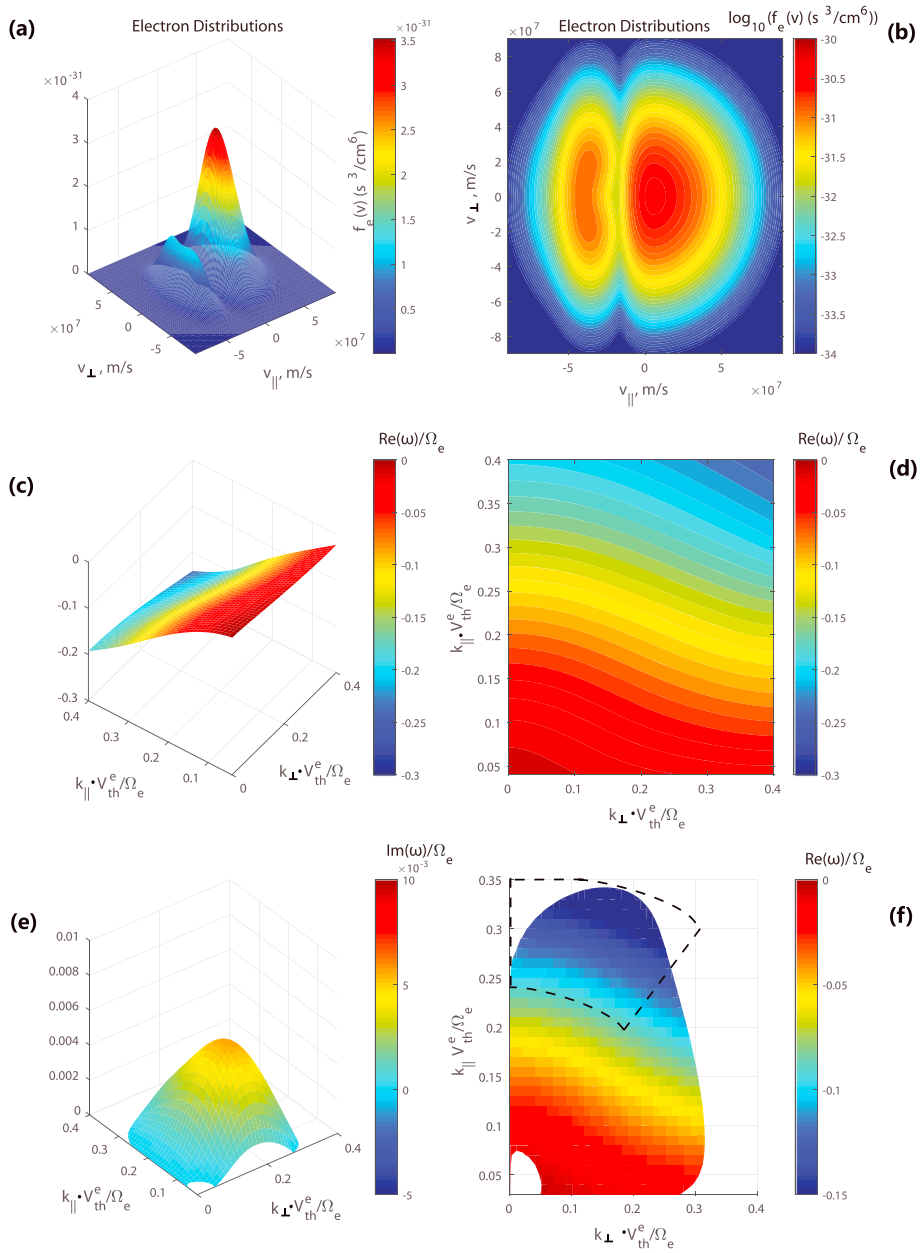

Figure 4. Numerical modeling of whistler waves growth in the events. (a, b) The modeled distribution of electrons with a field-aligned crescent in the antiparallel direction. (c, d) The dispersion surface of the whistler waves. (e, f) The growth rate of the whistler waves. The region surrounded by dashed lines indicates the parameter space in the observations. V_{th}^{e} is 3.24×10^{4} km/s, the thermal spread of the core population. The normalization constant $V_{\mathrm{th}}^{e}/\Omega_{e}$ is 15.3 km.

The "bump" distribution associated with field-aligned crescents is also unstable to electrostatic waves (Kennel, 1966; An et al., 2017). During our events, we observed electrostatic wave power in a broadband frequency range from the electron gyrofrequency to above the electron plasma frequency (supporting information). The electrostatic wave power can be associated with field-aligned beams and crescents. The energy dissipation into electrostatic wave power is subjected to future investigations.

3. Conclusions and Discussions

Whistler waves associated with field-aligned electron crescent-like beam are observed by MMS near the ion diffusion region of a near-Earth magnetotail reconnection. The propagation of the whistler waves and

the field-aligned electron crescents/beam is antiparallel to **B** and outward from the reconnection site. The field-aligned electron crescents produce an inverse slope ($\mathrm{d}f/\mathrm{d}|v_{||}| > 0$) at 1–5 keV in the velocity distribution. In the velocity space, the parallel propagation velocity of the whistler wave is in the range (1–5 keV) of the inverse slope of the field-aligned crescent/beam. The positive slope ($\mathrm{d}f/\mathrm{d}|v_{||}| > 0$) of the field-aligned crescents provides intense free energy at the $n = 0$ Landau resonance. On the other hand, the cyclotron resonance is at high-energy tail with negligible free energy of pitch angle anisotropy in these events. The numerical modeling and observations demonstrate that the whistler wave generation is due to the $n = 0$ Landau resonance. The corresponding growth rate of whistler waves from the Landau resonance is estimated as $\gamma/\Omega_e \sim 0.001$. The observed whistler waves power occur within very short (a few seconds) and discrete intervals, indicating a similar temporal feature of the free energy source of the waves.

Our results suggest that field-aligned electron crescents/beam dissipate significant free energy into whistler waves on a timescale of ~1,000 electron gyroperiods. Considering that the field-aligned electron crescent streams at about the electron Alfven speed in observations, the timescale is equivalent to a spatial scale of ~1,000 electron inertial length.

Acknowledgments
We appreciate the MMS team and the MMS Science Data Center (https://lasp.colorado.edu/mms/sdc/public/) for providing the MMS data for this study. The work at NSSC is supported by NNSFC grants 41874175, 41574161, 41731070, and 41574159 and the Strategic Pionner Program on Space Science II, Chinese Academy of Sciences, grants XDA15350201 and XDA15052500. W. L. would like to acknowledge the Alfred P. Sloan Research Fellowship FG-2018-10936. The French involvement (SCM instruments) on MMS is supported by CNES and CNRS.

References

An, X., Bortnik, J., Van Compernolle, B., Decyk, V., & Thorne, R. (2017). Electrostatic and whistler instabilities excited by an electron beam. *Physics of Plasmas*, *24*(7), 72,116.

An, X., Van Compernolle, B., Bortnik, J., Thorne, R. M., Chen, L., & Li, W. (2016). Resonant excitation of whistler waves by a helical electron beam. *Geophysical Research Letters*, *43*, 2413–2421. https://doi.org/10.1002/2015GL067126

Artemyev, A., Agapitov, O., Mourenas, D., Krasnoselskikh, V., Shastun, V., & Mozer, F. (2016). Oblique whistler-mode waves in the earth's inner magnetosphere: Energy distribution, origins, and role in radiation belt dynamics. *Space Science Reviews*, *200*(1–4), 261–355.

Blake, J. B., Mauk, B. H., Baker, D. N., Carranza, P., Clemmons, J. H., Craft, J., et al. (2016). The fly's eye energetic particle spectrometer (FEEPS) sensors for the magnetospheric multiscale (MMS) mission. *Space Science Reviews*, *199*, 309–329.

Burch, J. L., Torbert, R. B., Phan, T. D., Chen, L.-J., Moore, T. E., Ergun, R. E., et al. (2016). Electron-scale measurements of magnetic reconnection in space. *Science*, *352*, aaf2939. https://doi.org/10.1126/science.aaf2939

Burch, J. L., Webster, J. M., Genestreti, K. J., Torbert, R. B., Giles, B. L., Fuselier, S. A., et al. (2018). Wave phenomena and beam-plasma interactions at the magnetopause reconnection region. *Journal of Geophysical Research: Space Physics*, *123*, 1118–1133. https://doi.org/10.1002/2017JA024789

Cao, D., Fu, H. S., Cao, J. B., Wang, T. Y., Graham, D. B., Chen, Z. Z., et al. (2017). MMS observations of whistler waves in electron diffusion region. *Geophysical Research Letters*, *44*, 3954–3962. https://doi.org/10.1002/2017GL072703

Cattell, C., Wygant, J. R., Goetz, K., Kersten, K., Kellogg, P. J., von Rosenvinge, T., et al. (2008). Discovery of very large amplitude whistler-mode waves in Earth's radiation belts. *Geophysical Research Letters*, *35*, L01105. https://doi.org/10.1029/2007GL032009

Dai, L. (2009). Collisionless magnetic reconnection via Alfvén eigenmodes. *Physical Review Letters*, *102*, 245003. https://doi.org/10.1103/PhysRevLett.102.245003

Dai, L. (2018). Structures of Hall fields in asymmetric magnetic reconnection. *Journal of Geophysical Research: Space Physics*, *123*, 7332–7341. https://doi.org/10.1029/2018JA025251

Dai, L., Wang, C., Angelopoulos, V., & Glassmeier, K. (2015). In situ evidence of breaking the ion frozen-in condition via the non-gyrotropic pressure effect in magnetic reconnection. *Annales Geophysicae*, *33*(9), 1147–1153.

Dai, L., Wang, C., Zhang, Y., Lavraud, B., Burch, J., Pollock, C., & Torbert, R. B. (2017). Kinetic Alfvén wave explanation of the Hall fields in magnetic reconnection. *Geophysical Research Letters*, *44*, 634–640. https://doi.org/10.1002/2016GL071044

Dai, L., Wygant, J. R., Cattell, C., Dombeck, J., Thaller, S., Mouikis, C., et al. (2011). Cluster observations of surface waves in the ion jets from magnetotail reconnection. *Journal of Geophysical Research*, *116*, A12227. https://doi.org/10.1029/2011JA017004

Dai, L., Wygant, J. R., Cattell, C. A., Thaller, S., Kersten, K., Breneman, A., & Tang, X. (2014). Cluster observations of fast magnetosonic waves in the heliosphere current sheet. *Geophysical Research Letters*, *41*, 1398–1405. https://doi.org/10.1002/2014GL059223

Duan, S., Dai, L., Wang, C., He, Z., Cai, C., Zhang, Y. C., et al. (2017). Oxygen ions O+ energized by kinetic Alfvén eigenmode during dipolarizations of intense substorms. *Journal of Geophysical Research: Space Physics*, *122*, 11,256–11,273. https://doi.org/10.1002/2017JA024418

Duan, S., Dai, L., Wang, C., Liang, J., Lui, A. T. Y., Chen, L. J., et al. (2016). Evidence of kinetic Alfvén eigenmode in the near-Earth magnetotail during substorm expansion phase. *Journal of Geophysical Research: Space Physics*, *121*, 4316–4330. https://doi.org/10.1002/2016JA022431

Ergun, R. E., Tucker, S., Westfall, J., Goodrich, K. A., Malaspina, D. M., Summers, D., et al. (2016). The axial double probe and fields signal processing for the MMS mission. *Space Science Reviews*, *199*, 167–188.

Fu, H., Cao, J. B., Cully, C. M., Khotyaintsev, Y. V., Vaivads, A., Angelopoulos, V., et al. (2014). Whistler-mode waves inside flux pileup region: Structured or unstructured? *Journal of Geophysical Research: Space Physics*, *119*, 9089–9100. https://doi.org/10.1002/2014JA020204

Fujimoto, K. (2014). Wave activities in separatrix regions of magnetic reconnection. *Geophysical Research Letters*, *41*, 2721–2728. https://doi.org/10.1002/2014GL059893

Goldman, M., Newman, D., Lapenta, G., Andersson, L., Gosling, J., Eriksson, S., et al. (2014). Čerenkov emission of quasiparallel whistlers by fast electron phase-space holes during magnetic reconnection. *Physical Review Letters*, *112*(14), 145,002.

Graham, D. B., Vaivads, A., Khotyaintsev, Y. V., & Andre, M. (2016). Whistler emission in the separatrix regions of asymmetric magnetic reconnection. *Journal of Geophysical Research: Space Physics*, *121*, 1934–1954. https://doi.org/10.1002/2015JA021239

Hones, E. W. (1976). Observations in the Earth's magnetotail relating to magnetic merging. *Solar Physics*, *47*, 101.

Hoshino, M., Mukai, T., Terasawa, T., & Shinohara, I. (2001). Suprathermal electron acceleration in magnetic reconnection. *Journal of Geophysical Research*, *106*(A11), 25,979–25,997.

Huang, S. Y., Fu, H. S., Yuan, Z. G., Vaivads, A., Khotyaintsev, Y. V., Retino, A., et al. (2016). Two types of whistler waves in the Hall reconnection region. *Journal of Geophysical Research: Space Physics*, *121*, 6639–6646. https://doi.org/10.1002/2016JA022650

Huang, H., Yu, Y., Dai, L., & Wang, T. (2018). Kinetic Alfvén waves excited in two-dimensional magnetic reconnection. *Journal of Geophysical Research: Space Physics*, *123*, 6655–6669. https://doi.org/10.1029/2017JA025071

Kennel, C. (1966). Low-frequency whistler mode. *Physics of Fluids*, *9*(11), 2190–2202.

Le Contel, O., Leroy, P., Roux, A., Coillot, C., Alison, D., Bouabdellah, A., et al. (2016). The search-coil magnetometer for MMS. *Space Science Reviews*, *199*, 257–282.

Le Contel, O., Retinò, A., Breuillard, H., Mirioni, L., Robert, P., Chasapis, A., et al. (2016). Whistler mode waves and Hall fields detected by MMS during a dayside magnetopause crossing. *Geophysical Research Letters*, *43*, 5943–5952. https://doi.org/10.1002/2016GL068968

Li, J., Bortnik, J., An, X., Li, W., Russell, C. T., Zhou, M., et al. (2018). Local excitation of whistler mode waves and associated Langmuir waves at dayside reconnection regions. *Geophysical Research Letters*, *45*, 8793–8802. https://doi.org/10.1029/2018GL078287

Li, W., Mourenas, D., Artemyev, A. V., Bortnik, J., Thorne, R. M., Kletzing, C. A., et al. (2016). Unraveling the excitation mechanisms of highly oblique lower band chorus waves. *Geophysical Research Letters*, *43*, 8867–8875. https://doi.org/10.1002/2016GL070386

Lindqvist, P.-A., Olsson, G., Torbert, R. B., King, B., Granoff, M., Rau, D., et al. (2016). The spin-plane double probe electric field instrument for MMS. *Space Science Reviews*, *199*(1–4), 137–165.

Nagai, T., Fujimoto, M., Saito, Y., Machida, S., Terasawa, T., Nakamura, R., et al. (1998). Structure and dynamics of magnetic reconnection for substorm onsets with Geotail observations. *Journal of Geophysical Research*, *103*, 4419–4440. https://doi.org/10.1029/97JA02190

Narita, Y. (2017). Review article: Wave analysis methods for space plasma experiment. *Nonlinear Processes in Geophysics*, *24*(2), 203–214. https://doi.org/10.5194/npg-24-203-2017

Pollock, C. J., Moore, T., Jacques, A., Burch, J., Gliese, U., Saito, Y., et al. (2016). Fast plasma investigation for magnetospheric multiscale. *Space Science Reviews*, *199*, 331–406.

Russell, C., Anderson, B. J., Baumjohann, W., Bromund, K. R., Dearborn, D., Fischer, D., et al. (2016). The magnetospheric multiscale magnetometers. *Space Science Reviews*, *199*(1–4), 189–256.

Santolík, O., Parrot, M., & Lefeuvre, F. (2003). Singular value decomposition methods for wave propagation analysis. *Radio Science*, *38*(1), 1010. https://doi.org/10.1029/2000RS002523

Sonnerup, B. U. Ö., & Scheible, M. (1998). Minimum and maximum variance analysis. *ISSI Scientific Reports Series*, *1*, 185–220.

Tang, X., Cattell, C., Dombeck, J., Dai, L., Wilson, L. B., Breneman, A., & Hupach, A. (2013). THEMIS observations of the magnetopause electron diffusion region: Large amplitude waves and heated electrons. *Geophysical Research Letters*, *40*, 2884–2890. https://doi.org/10.1002/grl.50565

Torbert, R. B., Russell, C. T., Magnes, W., Ergun, R. E., Lindqvist, P.-A., Le Contel, O., et al. (2016). The fields instrument suite on MMS: Scientific objectives, measurements, and data products. *Space Science Reviews*, *199*, 105–135.

Tsurutani, B. T., & Smith, E. J. (1977). Two types of magnetospheric elf chorus and their substorm dependences. *Journal of Geophysical Research*, *82*(32), 5112–5128.

Wei, X. H., Cao, J. B., Zhou, G. C., SantolíK, O., RèMe, H., Dandouras, I., et al. (2007). Cluster observations of waves in the whistler frequency range associated with magnetic reconnection in the Earth's magnetotail. *Journal of Geophysical Research*, *112*, A10225. https://doi.org/10.1029/2006JA011771

Wilder, F. D., Ergun, R. E., Goodrich, K. A., Goldman, M. V., Newman, D. L., Malaspina, D. M., et al. (2016). Observations of whistler mode waves with nonlinear parallel electric fields near the dayside magnetic reconnection separatrix by the magnetospheric multiscale mission. *Geophysical Research Letters*, *43*, 5909–5917. https://doi.org/10.1002/2016GL069473

Wilder, F. D., Ergun, R. E., Newman, D. L., Goodrich, K. A., Trattner, K. J., Goldman, M. V., et al. (2017). The nonlinear behavior of whistler waves at the reconnecting dayside magnetopause as observed by the magnetospheric multiscale mission: A case study. *Journal of Geophysical Research: Space Physics*, *122*, 5487–5501. https://doi.org/10.1002/2017JA024062

Wilson, L. B., Cattell, C. A., Kellogg, P. J., Wygant, J. R., Goetz, K., Breneman, A., & Kersten, K. (2011). The properties of large amplitude whistler mode waves in the magnetosphere: Propagation and relationship with geomagnetic activity. *Geophysical Research Letters*, *38*, L17107. https://doi.org/10.1029/2011GL048671

Yoo, J., Jara-Almonte, J., Yerger, E., Wang, S., Qian, T., Le, A., et al. (2018). Whistler wave generation by anisotropic tail electrons during asymmetric magnetic reconnection in space and laboratory. *Geophysical Research Letters*, *45*, 8054–8061. https://doi.org/10.1029/2018GL079278

Zhang, Y. C., Lavraud, B., Dai, L., Wang, C., Marchaudon, A., Avanov, L., et al. (2017). Quantitative analysis of a Hall system in the exhaust of asymmetric magnetic reconnection. *Journal of Geophysical Research: Space Physics*, *122*, 5277–5289. https://doi.org/10.1002/2016JA023620

Zhang, L., Liu, Z., Ma, Z., Baumjohann, W., Pu, Z., Dunlop, M., et al. (2010). X line distribution determined from earthward and tailward convective bursty flows in the central plasma sheet. *Journal of Geophysical Research*, *115*, A06218. https://doi.org/10.1029/2009JA014429

Zhang, L., Lui, A., Baumjohann, W., & Wang, J. (2015). Probabilities of magnetic reconnection encounter at different activity levels in the Earth's magnetotail. *Advances in Space Research*, *56*(4), 736–741.

Zhang, Y., Matsumoto, H., & Kojima, H. (1999). Whistler mode waves in the magnetotail. *Journal of Geophysical Research*, *104*(A12), 28,633–28,644.

Zhou, M., Pang, Y., Deng, X. H., Yuan, Z., & Huang, S. Y. (2011). Density cavity in magnetic reconnection diffusion region in the presence of guide field. *Journal of Geophysical Research*, *116*, A06222. https://doi.org/10.1029/2010JA016324